GSA DATA REPOSITORY 2013154 G.J. Crutchley et al.

Supplement A: 3-D seismic data (technical methods):

The seismic cube was acquired in 2008 with the P-Cable 3D seismic system aboard the R/V Thomas Thompson and covers an area of 3 by 6 km (Bangs et al., 2011). The source consisted of two 300 in^3 airguns fired on a six second interval, resulting in an average shot spacing of ~12 m. 10 single channel analogue streamers were towed at ~1 m depth. Data processing in this study, which made use of GMT (Wessel and Smith, 1998), seismic unix (Stockwell and Cohen, 2008) and other commercial packages, was carried out with an emphasis on increasing the spatial resolution. The flow included channel repositioning, tidal corrections, trace editing and interpolation, and post-stack depth migration based on velocity information from both ocean bottom seismometers and long-offset 2D data (OR89 survey).

We calculated receiver geometry by assuming that the cross-cable of the P-Cable system adopts a catenary form as it is towed through the water column (Crutchley et al., 2011). This geometry was then fine-tuned by considering first arrival times that were converted to distances by assuming a water velocity of 1500 m/s. Static corrections were applied to account for tidal variations throughout the survey. Rigorous trace cleaning was required to remove spikes in the data. Much of the noise could be removed by applying a low-cut (50 Hz) frequency filter, but persistent noise bursts had to be removed by de-spiking routines and also by hand. Normal move-out was applied with a constant velocity of 1500 m/s and traces were then binned and stacked on a 12 m by 12 m grid. A post-stack interpolation routine was then applied in both the in-line and cross-line directions to reduce spatial aliasing, allowing the 3D migration routine to be more effective at collapsing diffractions. The result of the interpolation algorithm was a dataset with 6 m by 6 m spatial resolution, which was then migrated with a 3D, true-amplitude, post-stack, Kirchhoff time migration. The cube was then used to correlate broad geological features to 2D seismic profiles within the survey area where we also defined velocity models from a high-resolution arrangement of ocean-bottom seismometers. From this correlation we constructed a smooth 3D velocity model within the survey area that enabled us to carry out a post-stack depth migration. As a result, key horizons could be mapped in depth and used for fluid flow modeling.

Supplement B: Side-scan sonar data:

As a supplement to the seafloor similarity given in Figure 2B, we have included side-scan sonar data from the same area, which also highlight the NE-trending seepage area, as well as NE-trending faults farther to the west (Figure DR1). The data were acquired during cruise SO165 aboard R/V Sonne in 2001. Four successful deployments of the DTS-1 EgdeTech system during the cruise resulted in seven N-S trending profiles that were processed to create a mosaic image of the ridge.

Figure DR1 (see attached files). Comparison between seismic similarity from the seafloor reflection (**A**) and side-scan sonar data (**B**) from the same area. The same key features can be identified in both the seismic data and the side-scan sonar data – **A´ and B´** give interpretations of (A) and (B), respectively.

Supplement C: Fluid flow modeling:

Figure DR2 (see attached files). 3D views of the finite element mesh used for the fluid flow simulations. **A)** The broken white line is the BSR, marking the base of gas hydrate stability (BGHS). The red region of the mesh is the gas hydrate stability zone (GHSZ). The thin yellow region is Horizon A, both beneath the BSR and above the BSR. The blue region is model space beneath the BSR. The seafloor is the top of the red region – the Pinnacle location is annotated. **B)** The same field of view as (A) but the regions above the BSR have been stripped back to show the HA-BSR intersection – i.e. the intersection between Horizon A and the BSR.

We used the finite element-based, complex systems modelling platform (CSMP++, Matthäi et al., 2007) to simulate two-phase (methane gas and saline water) fluid flow within 3D geological models. Our approach is the same as that presented in Crutchley et al. (2010), but extended from 2D to 3D. CSMP++ is an unstructured finite-element code that has been developed to simulate fluid flow in structurally complex settings where geological features exist on vastly different length scales. We developed a high-resolution 3D finite-element model (Figure DR2) directly from horizons mapped out in depth from the seismic cube in order to represent the key geological features beneath South Hydrate Ridge. The model, which is 1440 m long, 680 m wide, and 1300 m deep (including the water column), contains ~290,000 tetrahedral elements with local refinement around horizon intersections and narrow layers. For example, Horizon A was modelled as a 5 m thick layer. We did not include the fractures in our model, as we aimed to test overpressure generation in the absence of these structures, which likely formed as a result of anomalous overpressure. The results show that the fractures are not required to focus fluid flow to beneath the Pinnacle.

As a first step, we solved the steady state expression for heat conduction to calculate the geothermal gradient throughout the model:

$$\nabla \cdot (K \nabla T) = 0, \qquad (1)$$

where K is the thermal conductivity of the fluid saturated sediments (J kg^{-3} s^{-1}) and T is the temperature (°C). Equation 1 was solved for constant basal heat flow, with temperature at the seafloor kept constant. Next, we solved the pressure diffusion equation (Geiger et al., 2006):

$$\nabla\left[k\left(\frac{k_{rw}}{\mu_w}\rho_w + \frac{k_{rg}}{\mu_g}\rho_g\right)\nabla P\right] + k\left(\frac{k_{rw}}{\mu_w}\rho_w{}^2 + \frac{k_{rg}}{\mu_g}\rho_g{}^2\right)g\nabla z = 0 \ , \qquad (2)$$

under steady state pressure conditions. In Equation 2, k is bulk permeability (m^2), k_{rw} is the relative permeability of water (-), μ_w is water viscosity (Pa·s), ρ_w is water density (kg m^{-3}), k_{rg} is the relative permeability of methane gas (-), μ_g is methane gas viscosity (Pa s), ρ_g is methane gas density (kg m^{-3}), P is pressure (Pa), g is the gravity constant (m s^{-2}), and z is the depth in the model (m). The solution to Equation 2 gives the fluid pressure distribution throughout the model. Relative permeabilities of saline water k_{rw} and methane gas k_{rg} (inputs to Equation 2) were calculated as a Corey-type non-linear function of their relative saturations – S_w and S_g, respectively, by assuming negligible residual saturations of water and gas (Geiger et al., 2006):

$$k_{rw} = \left(S_w\right)^4, \quad (3)$$

$$k_{rg} = \left(1 - S_w\right)^2\left(1 - \left(S_w\right)^2\right). \quad (4)$$

Fluid properties of the brine present in the pores (viscosity, compressibility and density) were calculated throughout the model from an equation of state for NaCl-H2O fluids, which accounts for temperature, pressure, and salinity (Driesner, 2007; Driesner and Heinrich, 2007). Methane density and viscosity were calculated according to ambient temperature and pressure throughout the model (Reid et al., 1987).

Parameterisation of the model and testing parameter ranges to verify results (Figure DR3):

We applied a large range of geologically plausible and consistent boundary conditions and parameter ranges to the model and its internal regions in order to simulate different possibilities and check the reliability of our results. The results presented in the paper (Figure 4) are from the most conservative of these models, where we assume uniform permeability throughout the entire model and a gas saturation of 40% within Horizon A beneath the base of gas hydrate stability. The uniform permeability value we use (2.3 x 10^{-15} m^2) is chosen to be appropriate for the approximate depth of Horizon A and the BGHS beneath the Pinnacle (the area of interest), according to the empirical relationship defined by Daigle and Dugan (2010) for Hydrate Ridge. We assume a conservative magnitude of upward fluid flux from the base of the model (1 x 10^{-8} kg m^2 s^{-1}), which is well below peak fluid flux measurements of several hundred mm/year measured during episodic flow on Hydrate Ridge (Tryon et al., 1999). All other fixed boundary conditions are outlined in Table 1. This model (Figure 4) is conservative because we do not simulate i) the effects of reduced permeability above the BGHS due to gas hydrate formation, nor ii) higher permeabilities in Horizon A. Both of these factors (‘i’ and ‘ii’) are, however, likely to be important. Firstly, Horizon A contains multiple coarse-grained, ash-rich turbidite beds (Tréhu et al., 2004) and is interpreted as being a (relatively) highly-permeable stratigraphic unit (Bangs et al., 2011). Secondly, gas hydrate forming in the pore space reduces the permeability of the host-rock (Kleinberg et al., 2003).

Table DR1: Fixed boundary conditions for all models

Parameter	**Units**	**Value**	**Model region**
Sediment density	kg m^{-3}	2500	Throughout
Thermal conductivity	W/(m K)	2.25	Throughout
Porosity	-	0.47	Throughout
Salinity	Wt%	3.2	Throughout
Fluid pressure	Pa	1.02 x 10^5	Sea level
Lithostatic pressure	Pa	1.02 x 10^5	Sea level
Temperature	°C	3	Sea level
Heat flux	W m^{-2}	0.04	Bottom boundary
Mass flux	kg m^2 s^{-1}	1 x 10^{-8}	Bottom boundary

Here, we show a range of results that takes into account these two factors. We simulate a reduction in permeability (Kleinberg et al., 2003) in response to a uniform gas hydrate saturation within the GHSZ of 2.0% (Hornbach et al., 2012). With respect to higher permeability in Horizon A, we simulate permeability higher than the surrounding sediments – i.e. one order of magnitude higher. To evaluate the influence of these results on our interpretations that overpressure develops around the HA-BSR intersection, we plot the pore fluid factor (λ_v) on Horizon A and compare it with the equivalent plot from the model given in the paper. The results (Figure DR3) underscore the reliability of the interpretations in this paper. That is, if Horizon A beneath the BSR is modelled as a gas charged layer (Tréhu et al., 2004), anomalous overpressure accumulates around the intersection between Horizon A and the BSR, largely independent of the permeability values assigned to individual rock layers. The magnitude of overpressure that is generated depends on how the model is parameterized (Figure DR3), but as we assume that the magnitude is sufficient to open hydrofractures and reactivate faults (Tréhu et al., 2004; Weinberger and Brown, 2006), we are more interested in where (spatially) this anomalous pressure accumulates. The results show that it accumulates around the HA-BSR intersection (Figure DR3).

Figure DR3 (see attached files). Maps of over-pressure (λ_v) distribution on Horizon A under varying model parameterisation. The sinuous double line marks the location of the HA-BSR intersection. **A)** λ_v distribution from the model displayed in Figure 4 of the paper (i.e. the “Base model”, which is the most conservative modelling scenario, where permeability is constant throughout the model). **B)** The Base model again (the same as A), with the same λ_v distribution, but the color scale is altered (λ_v spans 0.90-0.96, rather than 0.90-0.95, as in (A)) so that the results can be directly compared to the three test models shown in panels (C), (D) and (E). **C)** Model regions above the BSR and beneath the seafloor are allocated a reduced permeability representative of 2% gas hydrate saturation in the GHSZ, assuming a wall-coating mechanism of hydrate formation in the pore-space (Kleinberg et al., 2003). The result is a permeability reduction from 2.3 x 10^{-15} m^2 to 2.18 x 10^{-15} m^2 in gas hydrate bearing sediments. **D)** The model regions within Horizon A are allocated higher (i.e. one order of magnitude higher) permeability than surrounding sediments. **E)** Horizon A beneath the BSR is given a higher permeability, and sediments within the GHSZ are given lower permeability – i.e. a combination of the two different test models from (C) and (D).

Vertical fluid pressure sections (Figure DR4)

To show the steady state distribution of fluid overpressure in vertical sections through our model, we present results from a section extracted from one side of the HA-BSR intersection to the other (Figure DR4). Sub-panels A, B and C of Figure DR4 show fluid pressure fields from the model presented in Figure 4 in the paper. The vertical section in Figure DR4A shows anomalously high overpressure directly above the HA-BSR intersection, manifested as the down-bending of the overpressure field towards the HA-BSR intersection. In the absence of free gas within Horizon A beneath the BSR, the pressure field would be purely a function of depth, with λ_v contours running parallel to the seafloor. The down-bending of λ_v contours to the HA-BSR intersection in this model (Figure DR4A), where the influence of free gas is simulated, highlights the anomalously high fluid pressure between the BSR and the seafloor. Sub-figures DR4B and C show the overpressure field in this model extracted from Horizon A and the BSR, respectively. Sub-figure D shows the excess fluid pressure (in KPa) generated along the vertical section that is a result of the influence of free gas in Horizon A beneath the BSR. It is this excess fluid pressure that causes the down-bending of λ_v contours in (A).

Sub-Figures (E), (F) and (G) are from a model that we have parameterized differently from the base model results shown in sub-figures (A)-(D). In sub-figures (E)-(G) we have modelled lower fluid flux from the base of the model (5×10^{-9} kg m^2 s^{-1} rather than 1×10^{-8} kg m^2 s^{-1}), but locally higher fluid flux through Horizon A beneath the BSR (1×10^{-7} kg m^2 s^{-1}). We have also set the permeability in Horizon A beneath the BSR two orders of magnitude higher than permeability above the BSR in the gas hydrate-bearing sediments. This parameterisation is shown as an example of how higher fluid flux through Horizon A can lead to fluid overpressure around the BSR significantly in excess of lithostatic pressure. The key result here is that the spatial distribution of the highest fluid overpressure on both Horizon A and on the BSR (sub-figures F and G) is consistent with the results from the more conservative parameterisation of the model (sub-figures (B) and (C)). The highest overpressures on Horizon A occur along the HA-BSR intersection, and the highest overpressures on the BSR occur on the side of the HA-BSR intersection where Horizon A is beneath the BSR. These qualitative results are consistent with those of the most conservative model shown in Figure 4 of the paper, underscoring the stability of the model and our interpretations under extremely different parameterisations.

Figure DR4 (see attached files). A) Fluid overpressure (λ_v) plotted on a vertical section through the model that extends from one side (where Horizon A is below the BSR) to the other (where Horizon A is above the BSR). Horizon A is outlined by the yellow lines and the BSR is marked by the red lines. The HA-BSR intersection is given by the broken yellow line. The parameterisation of this model is the same as that of the model presented in Figure 4 in the paper (i.e. constant permeability throughout and 40% free gas saturation in Horizon A beneath the BSR). **B and C)** Overpressure distributions on Horizon A and on the BSR, respectively, from this same model. **D)** The excess fluid pressure field (in KPa) caused by the effect of having free gas in Horizon A beneath the BSR. The excess pressure plot here is the fluid pressure from (A) that is in excess of the background pressure field obtained by running the same model as (A) but without any free gas. **E)** Fluid overpressure (λ_v) plotted as in (A) but for a differently-parameterised model. Background permeability is 2.3×10^{-15} m^2, permeability above the BSR is 2.3×10^{-16} m^2, permeability within Horizon A beneath the BSR is 2.3×10^{-14} m^2. Basal fluid flux is 5×10^{-9} kg m^2 s^{-1}, whereas fluid flux through Horizon A is higher, at 1×10^{-7} kg m^2 s^{-1}. 40% gas saturation is again modelled in Horizon A beneath the BSR. **F and G)** Overpressure distributions on Horizon A and on the BSR, respectively, from this same model.

References:

Bangs, N.L.B., Hornbach, M.J., and Berndt, C., 2011, The mechanics of intermittent methane venting at South Hydrate Ridge inferred from 4D seismic surveying: Earth and Planetary Science Letters, v. 310, p. 105-112, doi:10.1016/j.epsl.2011.06.022.

Crutchley, G., Geiger, S., Pecher, I.A., Gorman, A.R., Zhu, H., and Henrys, S.A., 2010, The potential influence of shallow gas and gas hydrates on sea floor erosion of Rock Garden, an uplifted ridge offshore of New Zealand: Geo-Marine Letters, v. 30, p. 283-303.

Crutchley, G.J., Berndt, C.B., Klaeschen, D., and Masson, D.G., 2011, Insights into active deformation in the Gulf of Cadiz from new 3D seismic and high resolution bathymetry data: Geochemistry Geophysics Geosystems, v. 12, p. Q07016, doi:10.1029/2011GC003576.

Daigle, H., and Dugan, B., 2010, Origin and evolution of fracture-hosted methane hydrate deposits: Journal of Geophysical Research, v. 115, p. doi:10.1029/2010JB007492.

Driesner, T., 2007, The system H_2O–NaCl. Part II: Correlations for molar volume, enthalpy, and isobaric heat capacity from 0 to 1000 °C, 1 to 5000 bar, and 0 to 1 XNaCl: Geochimica et Cosmochimica Acta, v. 71, p. 4902–4919.

Driesner, T., and Heinrich, C.A., 2007, The system H_2O–NaCl. Part I: Correlation formulae for phase relations in temperature–pressure–composition space from 0 to 1000 °C, 0 to 5000 bar, and 0 to 1 XNaCl: Geochimica et Cosmochimica Acta, v. 71, p. 4880-4901.

Geiger, S., Driesner, T., Heinrich, C.A., and Matthäi, S.K., 2006, Multiphase Thermohaline Convection in the Earth's Crust: I. A New Finite Element – Finite Volume Solution Technique Combined With a New Equation of State for NaCl–H_2O: Transport in Porous Media, v. 63, p. 399-434.

Hornbach, M.J., Bangs, N.L., and Berndt, C., 2012, Detecting hydrate and fluid flow from bottom simulating reflector depth anomalies: Geology, v. 40, p. 227-230, doi: 10.1130/G32635.1.

Kleinberg, R.L., Flaum, C., Griffin, D.D., Brewer, P.G., Malby, G.E., Peltzer, E.T., and Yesinowski, J.P., 2003, Deep Sea NMR: Methane hydrate growth habit in porous media and its relationship to hydraulic permeability, deposit accumulation, and submarine slope stability: Journal of Geophysical Research, v. 108, p. 2508, doi: 10.1029/2003JB002389.

Matthäi, S.K., Geiger, S., Roberts, S.G., Paluszny, A., Belayneh, M., Burri, A., Mezentsev, A., Lu, H., Coumou, D., Driesner, T., and Heinrich, C.A., 2007, Numerical simulation of multi-phase fluid flow in structurally complex reservoirs, *in* Jolley, S.J., Barr, D., Walsh, J.J., and Knipe, R.J., eds., Structurally Complex Reservoirs, Volume 292, Geological Society, London, Special Publications, p. 405-429.

Reid, R.C., Prausnitz, J.M., and Poling, B.E., 1987, The Properties of Gases and Liquids: New York, McGraw Hill Book Company, 742 p.

Stockwell, J.W., and Cohen, J.K., 2008, The New SU User's Manual, Colorado School of Mines. Golden, CO 80401, USA.

Tréhu, A.M., Flemings, P.B., Bangs, N.L., Chevallier, J., Gràcia, E., Johnson, J.E., Liu, C.-S., Liu, X., Riedel, M., and Torres, M.E., 2004, Feeding methane vents and gas hydrate deposits at south Hydrate Ridge: Geophysical Research Letters, v. 31, p. 1-4.

Tryon, M.D., Brown, K.M., Torres, M.E., Trehu, A.M., McManus, J., and Collier, R.W., 1999, Measurements of transience and downward fluid flow near episodic methane gas vents, Hydrate Ridge, Cascadia: Geology, v. 27, p. 1075-1078.

Weinberger, J.L., and Brown, K.M., 2006, Fracture networks and hydrate distribution at Hydrate Ridge, Oregon: Earth and Planetary Science Letters, v. 245, p. 123-136.

Wessel, P., and Smith, W.H.S., 1998, New, improved version of the Generic Mapping Tools released: Eos Transactions, AGU, v. 79, p. 579.

Figure DR1

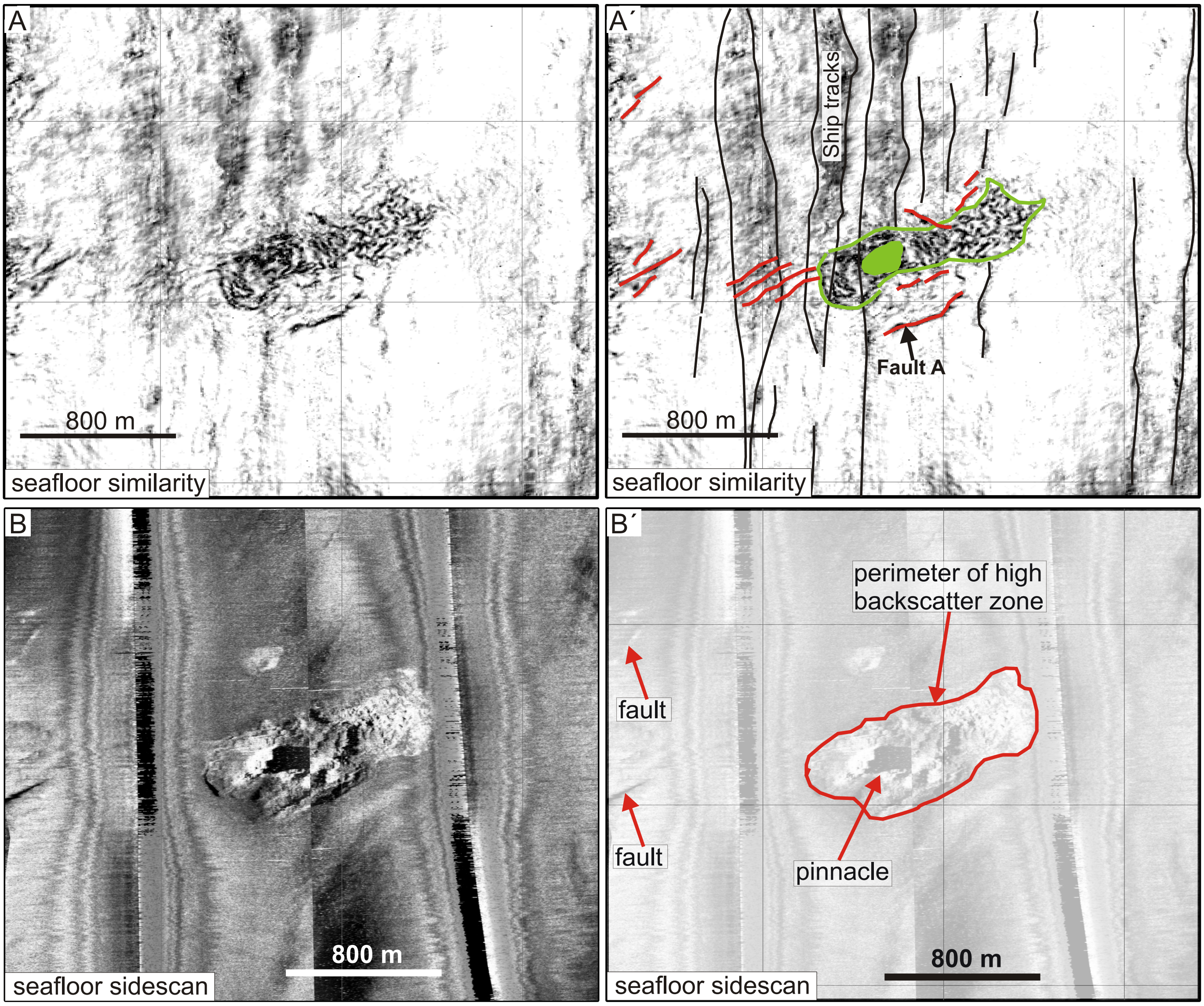
A
800 m
seafloor similarity
A´
Ship tracks
Fault A
800 m
seafloor similarity
B
800 m
seafloor sidescan
B´
perimeter of high backscatter zone
fault
fault
pinnacle
800 m
seafloor sidescan

Figure DR2

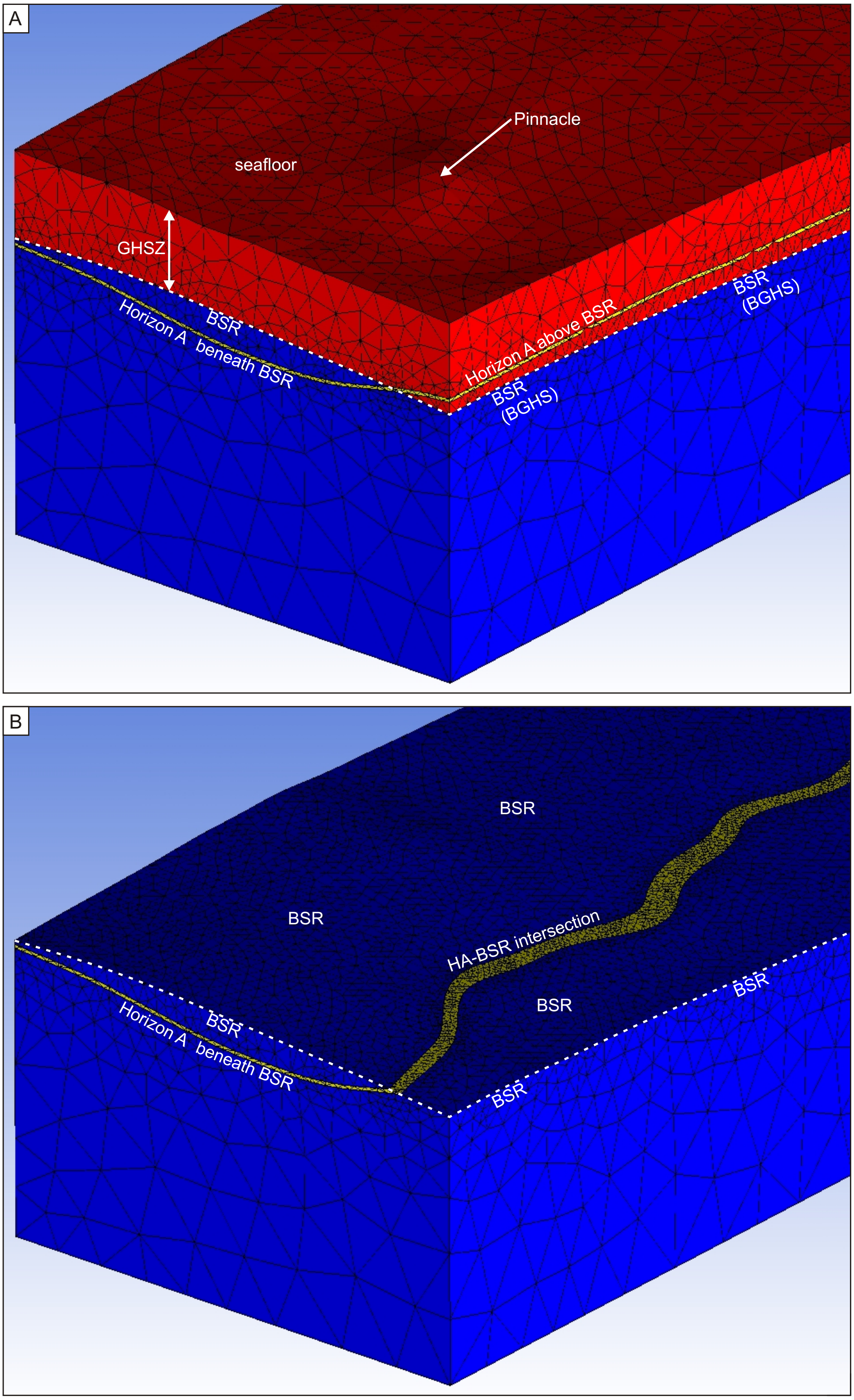
A
Pinnacle
seafloor
GHSZ
BSR
Horizon A
beneath BSR
Horizon A above BSR
BSR
(BGHS)
BSR
(BGHS)
B
BSR
BSR
HA-BSR intersection
BSR
BSR
Horizon A
beneath BSR
BSR
BSR

Figure DR3

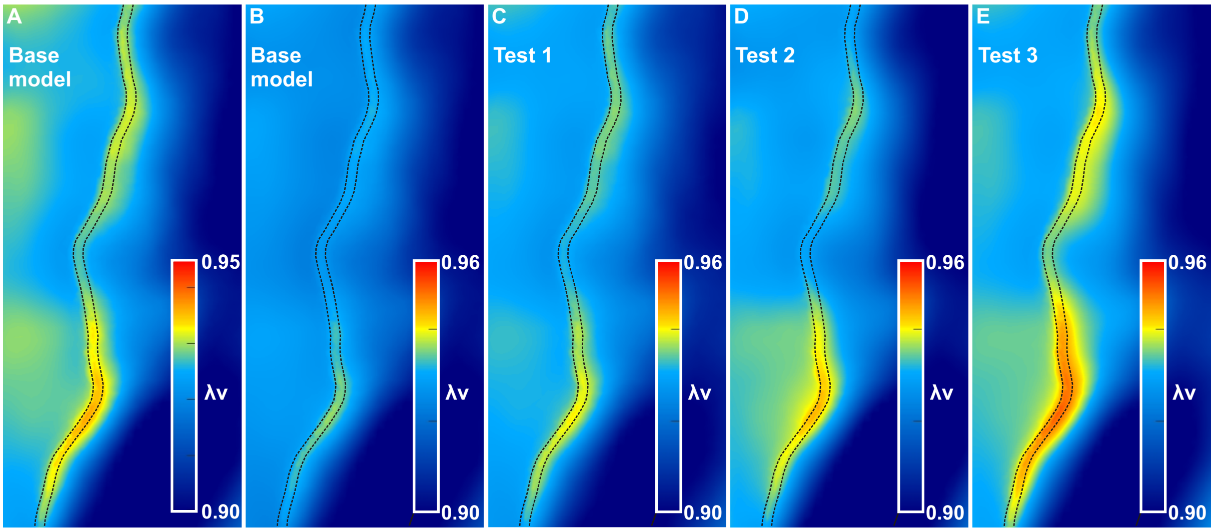
A
Base model
0.95
λv
0.90
B
Base model
0.96
λv
0.90
C
Test 1
0.96
λv
0.90
D
Test 2
0.96
λv
0.90
E
Test 3
0.96
λv
0.90

Figure DR4

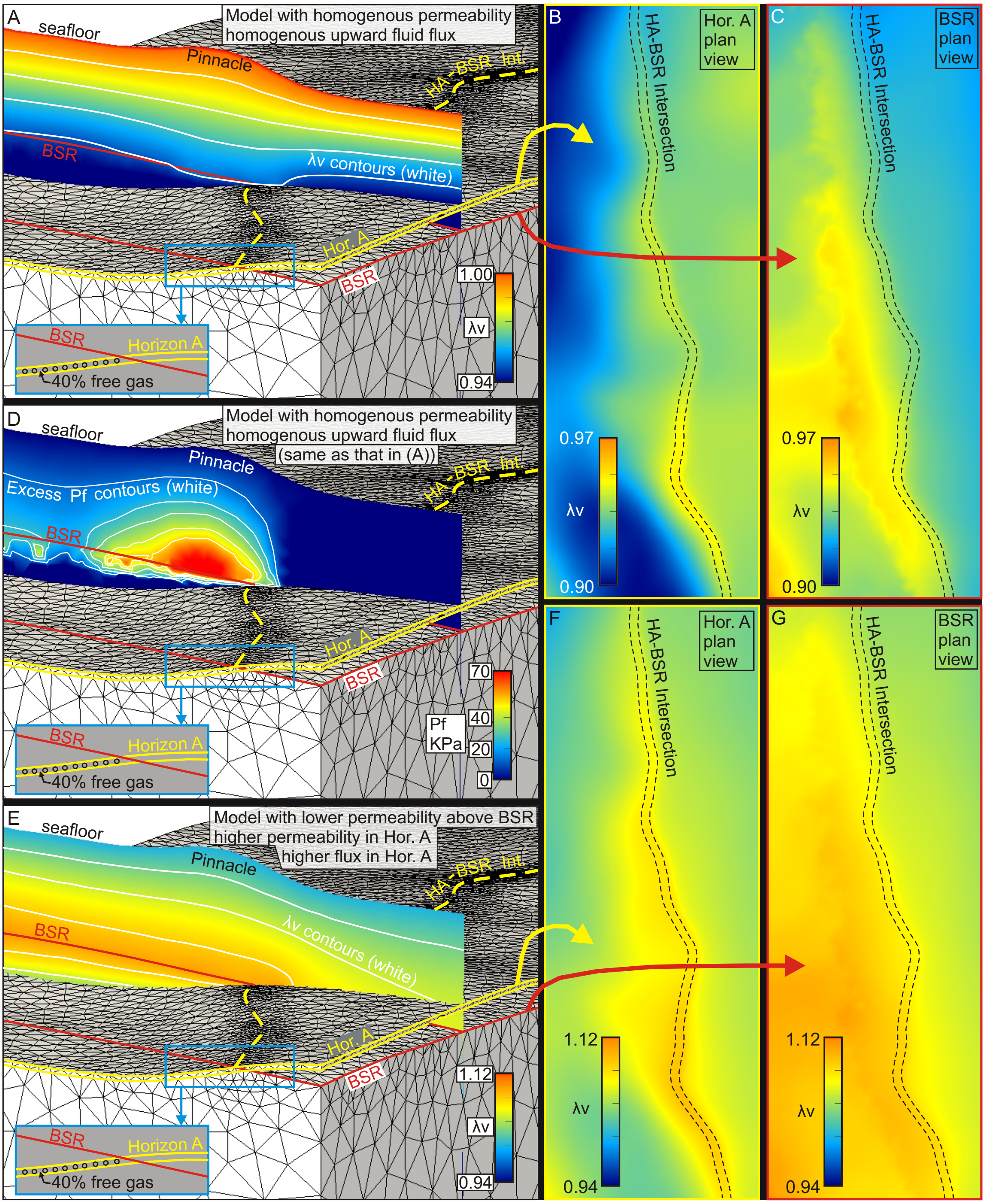
A
seafloor
Model with homogenous permeability
homogenous upward fluid flux
Pinnacle
HA-BSR Int.
BSR
λv contours (white)
Hor. A
BSR
1.00
λv
0.94
BSR
Horizon A
40% free gas
B
HA-BSR Intersection
Hor. A plan view
0.97
λv
0.90
C
HA-BSR Intersection
BSR plan view
0.97
λv
0.90
D
seafloor
Model with homogenous permeability
homogenous upward fluid flux
(same as that in (A))
Pinnacle
Excess Pf contours (white)
BSR
HA-BSR Int.
Hor. A
BSR
70
40
Pf KPa
20
0
BSR
Horizon A
40% free gas
E
seafloor
Model with lower permeability above BSR
higher permeability in Hor. A
higher flux in Hor. A
Pinnacle
HA-BSR Int.
BSR
λv contours (white)
Hor. A
BSR
1.12
λv
0.94
BSR
Horizon A
40% free gas
F
HA-BSR Intersection
Hor. A plan view
1.12
λv
0.94
G
HA-BSR Intersection
BSR plan view
1.12
λv
0.94